ADVANCED MATERIALS
www.advmat.de

Scalable Synthesis of Monolayer Hexagonal Boron Nitride on Graphene with Giant Bandgap Renormalization

Ping Wang, Woncheol Lee, Joseph P. Corbett, William H. Koll, Nguyen M. Vu, David Arto Laleyan, Qiannan Wen, Yuanpeng Wu, Ayush Pandey, Jiseok Gim, Ding Wang, Diana Y. Qiu, Robert Hovden, Mackillo Kira, John T. Heron, Jay A. Gupta, Emmanouil Kioupakis,* and Zetian Mi**

Monolayer hexagonal boron nitride (hBN) has been widely considered a fundamental building block for 2D heterostructures and devices. However, the controlled and scalable synthesis of hBN and its 2D heterostructures has remained a daunting challenge. Here, an hBN/graphene (hBN/G) interface-mediated growth process for the controlled synthesis of high-quality monolayer hBN is proposed and further demonstrated. It is discovered that the in-plane hBN/G interface can be precisely controlled, enabling the scalable epitaxy of unidirectional monolayer hBN on graphene, which exhibits a uniform moiré superlattice consistent with single-domain hBN, aligned to the underlying graphene lattice. Furthermore, it is identified that the deep-ultraviolet emission at 6.12 eV stems from the 1s-exciton state of monolayer hBN with a giant renormalized direct bandgap on graphene. This work provides a viable path for the controlled synthesis of ultraclean, wafer-scale, atomically ordered 2D quantum materials, as well as the fabrication of 2D quantum electronic and optoelectronic devices.

1. Introduction

The emerging 2D materials and their heterostructures have provided exciting prospects for the applications of next-generation electronic, photonic, and quantum devices.[1–5] Monolayer hexagonal boron nitride (hBN) and graphene,[6,7] the thinnest of all insulators and semimetals, respectively, have been considered as fundamental building blocks of such 2D devices. Specifically, vertically stacked hBN/graphene (hBN/G) van der Waals (vdW) heterostructures have been successfully employed to produce emergent properties, such as quantum Hall effect,[8] Hofstadter butterfly spectrum,[9] and plasmon and phonon polaritons.[10] Complementary to the vertical hBN/G vdW heterostructure, the in-plane version forms a covalent hBN/G heterostructure with equally attractive properties, such as transitions between semiconducting, half metallic, and metallic phases, spin polarization magnetism, and exotic electronic states,[11–15] or even the possibility to reconstruct electronic interfaces similar to those observed in oxide heterostructures.[16,17] The scope of these fascinating properties could be radically expanded by demonstrating epitaxially grown monolayer hBN on graphene with superior structural, electrical, and optical properties, as well as precise control of both the hBN/G out-of-plane and in-plane monolayer interfaces.

Recently, intensive efforts have been devoted to the epitaxial growth of hBN on metals,[18–20] sapphire,[21] and graphene substrates[22] by using sputtering,[23] chemical vapor deposition (CVD),[24] metal–organic chemical vapor deposition (MOCVD),[25] and molecular beam epitaxy (MBE).[26] Due to the

---

P. Wang, W. Lee, D. A. Laleyan, Q. Wen, Y. Wu, A. Pandey, D. Wang, M. Kira, Z. Mi
Department of Electrical Engineering and Computer Science
University of Michigan
Ann Arbor, MI 48109, USA
E-mail: ztmi@umich.edu

The ORCID identification number(s) for the author(s) of this article can be found under https://doi.org/10.1002/adma.202201387.

DOI: 10.1002/adma.202201387

J. P. Corbett, W. H. Koll, J. A. Gupta
Department of Physics
Ohio State University
Columbus, OH 43210, USA
E-mail: gupta.208@osu.edu

J. P. Corbett
UES Inc.
4401 Dayton-Xenia Rd, Dayton, OH 45432, USA

N. M. Vu, J. Gim, R. Hovden, J. T. Heron, E. Kioupakis
Department of Material Science and Engineering
University of Michigan
Ann Arbor, MI 48109, USA
E-mail: kioup@umich.edu

D. Y. Qiu
Department of Mechanical Engineering and Materials Science
Yale University
New Haven, CT 06516, USA

compatible lattice symmetry and small lattice mismatch (around 1.6%), highly oriented pyrolytic graphite (HOPG) and epitaxial graphene have emerged as promising substrates for the epitaxy of monolayer hBN as well as hBN/G heterostructures.[22,27–29] In addition, the moiré superlattice formed between epitaxially grown hBN/G heterostructures can be utilized to engineer correlated quantum electronic states in their vdW heterostructures.[30,31] However, the epitaxy of hBN/G heterostructures with controlled interface configuration has remained elusive. In addition, the recent experimentally measured 6.1 eV emission energy for monolayer hBN on graphene[32,33] differs greatly from the theoretically predicted 8 eV bandgap for freestanding monolayer hBN.[34–36] We introduce an interface-mediated synthesis of monolayer hBN on graphene as a viable path for the controlled synthesis of their 2D monolayer heterostructures on a wafer-scale. Our detailed theoretical calculations predict a giant bandgap renormalization and 0.7 eV exciton binding energy for monolayer hBN on graphene, matching our deep-ultraviolet (UV) photoluminescence (PL) measurements, which show an excitonic emission at 6.12 eV.

2. Results and Discussion

2.1. Interface-Mediated Synthesis of Monolayer hBN

Our growth concept is based on controlling hBN/G interface formation to create uniform active sites that promote precise hBN nucleation and eventually faultless, in-plane lateral epitaxy up to macroscopic scales. Unless controlled, graphene substrates unintentionally contain arbitrary mixtures of so-called armchair (AC) and zigzag (ZZ) atomic edges. This leads to a myriad of possible hBN/G in-plane interfaces. **Figure** 1a shows an $\mathrm{AC_G\|AC_{hBN}}$ interface and Figure 1b shows a $\mathrm{ZZ_G\|ZZ_{hBN}}$ interface, which is the two most likely ones due to the relatively low formation energy (Table S1, Supporting Information). Uncontrolled interfaces have so far prevented the precise and flexible synthesis of hBN/G heterostructures. The coexistence of these interfaces also makes the unidirectional hBN single-domain formation and controllable coalescence elusive. Theoretical calculations have suggested a smaller formation energy for $\mathrm{AC_G\|AC_{hBN}}$ interface (2.2 eV $\mathrm{nm^{-1}}$) compared to $\mathrm{ZZ_G\|ZZ_{hBN}}$ interface (2.8 eV $\mathrm{nm^{-1}}$),[11,12] indicating that $\mathrm{AC_G\|AC_{hBN}}$ interface is energetically more stable than $\mathrm{ZZ_G\|ZZ_{hBN}}$ interface, when grown under nearly thermal equilibrium conditions, such as ultrahigh growth temperatures. We exploit this difference to control the atomic configuration of the hBN/G interface. Based on the thermodynamic stability of hBN/G interfaces, we propose an interface-mediated synthesis method for MBE-grown hBN on graphene substrates, by suppressing the formation of $\mathrm{ZZ_G\|ZZ_{hBN}}$ interface. Specifically, we synthesize hBN/G under nearly thermal equilibrium conditions to grow exclusively $\mathrm{AC_G\|AC_{hBN}}$ interfaces, which makes unidirectional, superior quality hBN lateral epitaxy possible.

Under optimal conditions, a pristine hBN front grows along a single direction, in a single pattern, and from a single graphene atomic edge. The intermediate product will then be an hBN nanoribbon propagating to become a pristine monolayer hBN once its width becomes macroscopic. To control the actual growth conditions, we synthesize monolayer hBN on HOPG substrates using MBE at growth temperatures ranging from 800 to 1600 °C. Figure 1c–e and Figure S1, Supporting Information, show scanning electron microscopy (SEM) images characterizing the hBN growth; the light (dark) areas denote hBN (HOPG), the red dashed lines the hBN/graphene nucleation interfaces, and the white dashed lines the hBN growth fronts whose propagation direction is indicated by white dashed arrows. For the growth temperature of 1000 °C, nanoribbons start to grow in both directions from the graphene atomic edges. Moreover, different regions produce randomly either straight or jagged hBN nanoribbons, as shown by exemplary regions in insets of Figure 1c and Figure S2, Supporting Information. Similarly, imperfect growth behavior was observed at 1200 °C.

However, the growth mode starts to drastically change at 1400 °C producing a unidirectional growth from the graphene atomic edge to produce a uniform, ultraclean, and straight hBN nanoribbon as shown in Figure 1d, although some regions still show bidirectional growth. At 1600 °C, unidirectional growth dominates essentially all regions as shown in Figure 1e. All these straight nanoribbons are monolayer hBN with a thickness of 0.35 nm, a uniform width, and length up to sub-millimeter scale (Figure S3, Supporting Information). The evolution of hBN nanoribbons with growth duration is shown in Figure 1e–g. Nanoribbon width increases linearly with a 3 nm $\mathrm{min^{-1}}$ lateral growth rate. This can be exploited to grow macroscopic monolayer hBN if the graphene substrate contains a single graphene atomic edge. However, our HOPG substrates contain a high density of graphene atomic edges on the surface, producing terraces separated by hundreds of nanometers. Therefore, extending the growth time to 90 min still produces straight hBN nanoribbons forming wider hBN nanoribbons but are seamlessly stitched with the adjacent ones to finally form a large-area monolayer hBN—as seen in Figure 1g. Due to the nonuniform height (monolayer to multiple layers) of graphene atomic edges on HOPG, a new monolayer hBN may start to grow on top of the coalesced hBN along the initial graphene atomic edge, forming bilayer regions, as indicated by white solid arrows in Figure 1g. In addition, the nonuniform graphene atomic edges can also introduce grain boundaries (GBs) during the nanoribbons growth and coalescence (Figure 1g). By utilizing graphene substrates with well-isolated atomic edges, the proposed growth technique offers a viable path to achieve ultraclean, wafer-scale monolayer hBN and hBN/G heterostructures.

As discussed above, nonideal growth temperatures (≤1200 °C) often produce a bidirectional lateral hBN growth, which we attribute to the formation of BN nanoparticles (Figure 1c,d along the graphene atomic edges). At lower growth temperatures, boron adatoms tend to accumulate along the graphene edges due to the large diffusion length on graphene and relatively low desorption rate. They enable both in-plane and out-of-plane hBN/G interface formation. The higher growth temperatures dramatically suppress the BN nanoparticles formation, allowing only the energetically stable in-plane hBN/G interface to survive. As a result, hBN grows only on the in-plane side of graphene for the 1600 °C growth. In addition, the active nitrogen plasma may introduce defects in graphene,

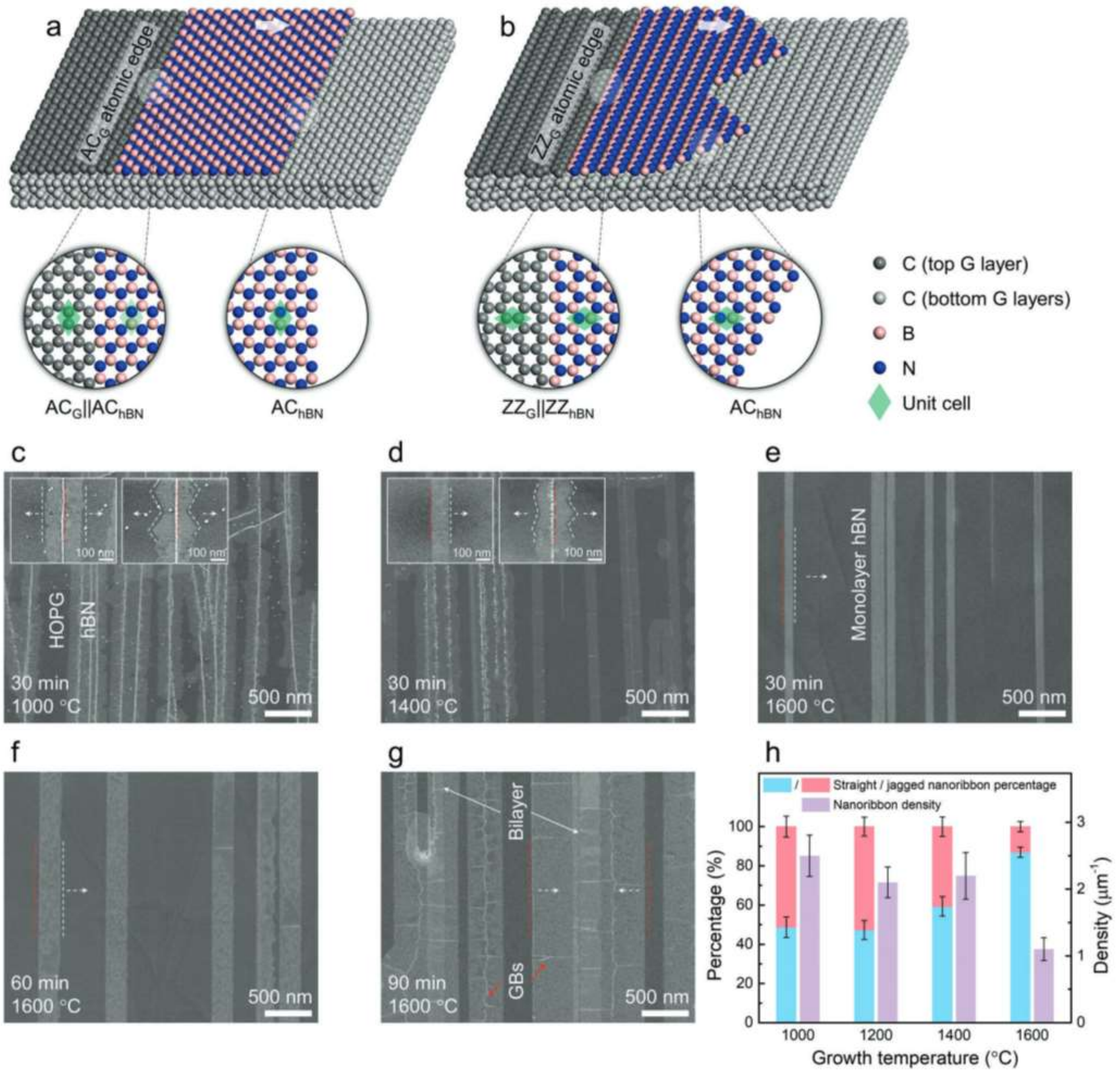

Figure 1. Concept and demonstration of interface-mediated synthesis of monolayer hBN. a,b) Schematics of monolayer hBN grown along the armchair (AC_G) (a) and zigzag (ZZ_G) (b) graphene atomic edges, forming straight and jagged nanoribbons, respectively. All growth fronts of monolayer hBN are terminated with AC_{hBN} edges. The magnifications show the atomic configurations of the $AC_G||AC_{hBN}$ and $ZZ_G||ZZ_{hBN}$ in-plane interfaces, and the AC_{hBN} growth fronts. The white arrows point to the growth direction. c–e) Typical SEM images of monolayer hBN nanoribbons morphology, grown along graphene atomic edges at 1000 °C (c), 1400 °C (d), and 1600 °C (e) for 30 min. The insets in (c,d) show the typical morphology of straight and jagged hBN nanoribbons. e–g) Evolution of straight monolayer hBN nanoribbons is followed after 30 min (e), 60 min (f), and 90 min (g) growth time at 1600 °C. The red dashed lines depict the hBN/graphene nucleation interfaces and the white dashed lines show the outline of hBN growth fronts; the white dashed arrows point to the growth direction. The white solid arrows indicate bilayer hBN formed from the initial hBN/graphene nucleation interfaces after underlying straight monolayer hBN nanoribbons coalescence; the red solid arrows show the GBs formed during nanoribbon growth and coalescence. h) Measured percentage of straight versus jagged hBN nanoribbons and nanoribbon density is shown as a function of growth temperature, demonstrating the dominance of straight nanoribbons (with well-defined $AC_G||AC_{hBN}$ in-plane interfaces) at a growth temperature of 1600 °C. The error bars show the standard deviation.

which have been experimentally confirmed in previous graphene-assisted III-nitrides growth.[37,38] However, we have not observed any negative impact of such defects on hBN nucleation and growth, which is likely due to the limited (point) defect size. High temperature annealing has been proposed as an effective approach to improving the crystallinity of hBN and the crystal quality of AlN.[39–42] We have also performed high-temperature annealing at 1600 °C in the same MBE

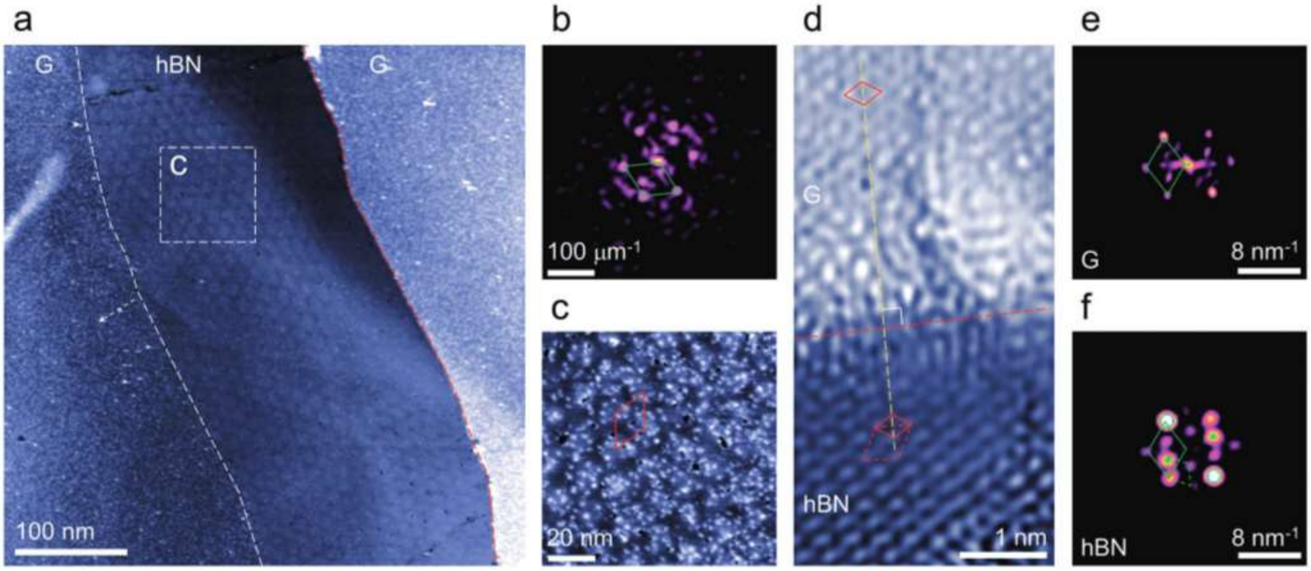

Figure 2. Epitaxial registry between monolayer hBN and graphene. a–c) Moiré superlattice with a single periodicity spanning the entire monolayer hBN region: a) STM image of a straight monolayer hBN nanoribbon (grown at 1600 °C for 60 min, Figure 1f), showing a clear moiré superlattice, b) the corresponding FFT, showing a hexagonal lattice, and c) magnified image of the white box in (a). The red dashed and white dashed lines in (a) depict the hBN/G nucleation interface and the outline of hBN growth front, respectively, and the white dashed arrow shows the growth direction. The green and red diamonds in (b) and (c) represent the unit cell of a moiré superlattice in reciprocal- and real-space, respectively. d–f) Nucleation interface atomic configuration for straight monolayer hBN nanoribbons: d) atomic-resolved STM image acquired from a straight monolayer hBN nanoribbon nucleation interface, and e,f) the corresponding FFTs for the graphene and hBN regions, respectively. The red solid and green solid (dashed) diamonds represent the corresponding unit (super) cell in real- and reciprocal-space, respectively. The red dashed line in (d) indicates the hBN/G nucleation interface, while the yellow dashed line shows the alignment of unit cells. They are perpendicular to each other. The $AC_G||AC_{hBN}$ interface configuration is unambiguously confirmed by comparing the experimentally measured unit cell alignment with the atomic model shown in Figure 1a.

chamber for the hBN samples grown at lower temperatures. However, the morphology of hBN nanoribbons, as well as the above-mentioned BN nanoparticles, barely change, which is attributed to the robust thermal stability of BN.

The quality of temperature-dependent hBN growth is quantified in Figure 1h in terms of straight and jagged nanoribbon fraction as well as nanoribbon density. At growth temperatures below 1200 °C, straight and jagged hBN nanoribbons have almost the same percentage 50%. As the growth temperature is increased to 1600 °C, the percentage of straight hBN nanoribbon significantly increases up to 87% and the nanoribbon density decreases almost to half compared to lower growth temperatures. This results from the suppressed growth of jagged hBN nanoribbons. In other words, we have demonstrated a highly selective growth of uniform, ultraclean, and straight hBN nanoribbons by utilizing ultrahigh growth temperature, close to the thermal equilibrium conditions. Notably, 100% selectivity should be achievable by further increasing the growth temperature.

To further quantify the hBN quality, we use scanning tunneling microscopy (STM) to image the monolayer hBN grown at 1600 °C for 60 min, corresponding to Figure 1f where straight nanoribbons have not yet coalesced into the complete monolayer hBN film. **Figure 2**a shows an STM image focused on a single nanoribbon. At this magnification, a uniform moiré superlattice is observed along the entire imaged length of the nanoribbon. The corresponding fast Fourier transform (FFT) (Figure 2b) shows a slightly distorted hexagonal reciprocal lattice, with an average spot separation corresponding to a periodicity of 16 nm. While the visibility of moiré superlattice varies with the STM tip termination, periodicities of 16 ± 1 nm are observed on nanoribbons in distinct areas of the sample (Figure 2c and Figure S4, Supporting Information). The measured moiré periodicity exceeds the maximum period of 14 nm, calculated using the bulk hBN lattice constant and rotational alignment with graphene.[30] The larger observed moiré period suggests that the monolayer hBN lattice is compressively strained to be more commensurate with the underlying graphene lattice. We can place bounds on the strain (> 0.2%) and twist angle (< 0.9°) from these measurements of the moiré superlattice. The slight compressive strain mainly arises from the in-plane covalent hBN/G heterostructure, in which the small lattice mismatch (1.6%) between hBN and graphene needs to be considered. These results corroborate the proposed growth model, and are consistent with nearly commensurate, single-domain hBN, aligned to the underlying graphene lattice.

To explore the interface-mediated epitaxy model, we present atomically resolved STM images close to the nucleation interface (red dashed line) in Figure 2d and growth front regions (Figure S5, Supporting Information) of the straight monolayer hBN nanoribbons. In Figure 2d, the parent graphene appears on the top of the image, with the hBN nanoribbon growing down toward the bottom. Though the two surfaces are nearly co-planar, the insulating hBN leads to darker contrast, corresponding to an apparent step down of 260 pm.

Atomic-scale contrast at the interface likely reflects defect states associated with hBN/G bonding, which makes it difficult to identify how the two honeycomb lattices are joined. However, the corresponding unit cells in real-space (red diamonds) and reciprocal-space (green diamonds) for the two regions show hexagonal periodicities that are aligned between graphene and hBN, as seen in Figure 2e,f. This demonstrates that hBN registers to the graphene atomic edge during the initial nucleation, consistent with the $AC_G \| AC_{hBN}$ interface model in Figure 1a. Atomic-resolution STM images of the hBN growth front (Figure S5, Supporting Information) exhibit similar alignment, consistent with growth aligned to the underlying graphene lattice. These results suggest that the survived straight monolayer hBN nanoribbons, when grown under ultrahigh temperatures, are initiated from the $AC_G \| AC_{hBN}$ interface, agreeing well with the proposed interface-mediated process.

Having confirmed the high-quality and single-domain nature of our monolayer hBN, we have further characterized the electrical and optical properties. Specifically, we find an excellent insulating property and electrical reliability on this epitaxial hBN via conductive atomic force microscopy (cAFM) (Figures S6 and S7, Supporting Information).

2.2. Deep-UV Emission of Epitaxial Monolayer hBN

The unique optical properties of monolayer hBN result from the extraordinary strong light-matter interaction.[33–35,43–46] Therefore, we characterize our hBN/HOPG samples further by using temperature-variable PL spectroscopy, as schematically shown in **Figure 3**a. The measured, time-integrated PL spectrum at 12 K (blue curve) and the reflectance spectrum at 300 K (red curve) are presented in Figure 3b for the monolayer hBN sample of Figure 1g. The dashed lines are the reference PL and reflectance spectra of a HOPG substrate alone. Evidently, the epitaxial hBN significantly affects the reflectance spectrum of HOPG in the high photon-energy range, with a pronounced dip at 6.12 eV compared to the monotonic decline of the HOPG substrate reflectance beyond 5.1 eV. This significant extinction of reflected light suggests a strong light-matter coupling with the presence of hBN.[32,47] The pronounced hBN resonance is further corroborated by the PL spectra; only the hBN/HOPG sample exhibits a sharp resonance at 6.12 eV (Figure 3b and Figure S8a, Supporting Information). This behavior changes dramatically for the lower-quality sample grown at 800 °C; it produces a broad defect-related emission below 5.6 eV (Figure S8b, Supporting Information), whereas our highest-quality sample completely suppresses the defect emission. Specifically, we observe three prominent peaks at 6.12, 6.01, and 5.86 eV, superimposed with a tail of HOPG PL, two of them originating from high-quality monolayer hBN, as discussed below.

To identify the physical origin of these three peaks, we measure time-integrated PL as a function of temperature T and construct the normalized peak values with respect to 12 K PL for each peak; see Figure S8c, Supporting Information, for temperature-dependent PL spectra. Figure 3c summarizes the T dependence of normalized PL peak intensity for the 6.12 (squares), 6.01 (circles), and 5.86 eV (triangles) peaks. The 6.12 eV peak intensity drops slightly until $T = 100$ K, and the 6.01eV peak decreases slowly until $T = 40$ K, whereas the 5.86 eV peak starts to rapidly drop already above 20 K. Both the peak position and T dependence intensity trend for 5.86 eV peak is similar to that observed in multilayer hBN.[48,49] Thus, we assign the 5.86 eV peak to multilayer hBN. At the same time, the 6.12 eV PL peak matches with a strong reflection resonance; in fact, it is the only one visible there, indicating it has by far the strongest light-matter coupling. Thus, we assign it to a monolayer hBN whose strongest confinement increases the light-matter coupling much beyond those of multilayer. The presence of both monolayer and multilayer hBN PL resonances is to be expected in the sample of Figure 1g containing multiple layer thicknesses. The 6.01 eV peak's T dependence is between multilayer and monolayer, which indicates it could be from defect-brightened emission in monolayer hBN;[32] this possibility is verified in the context of Figure 4.

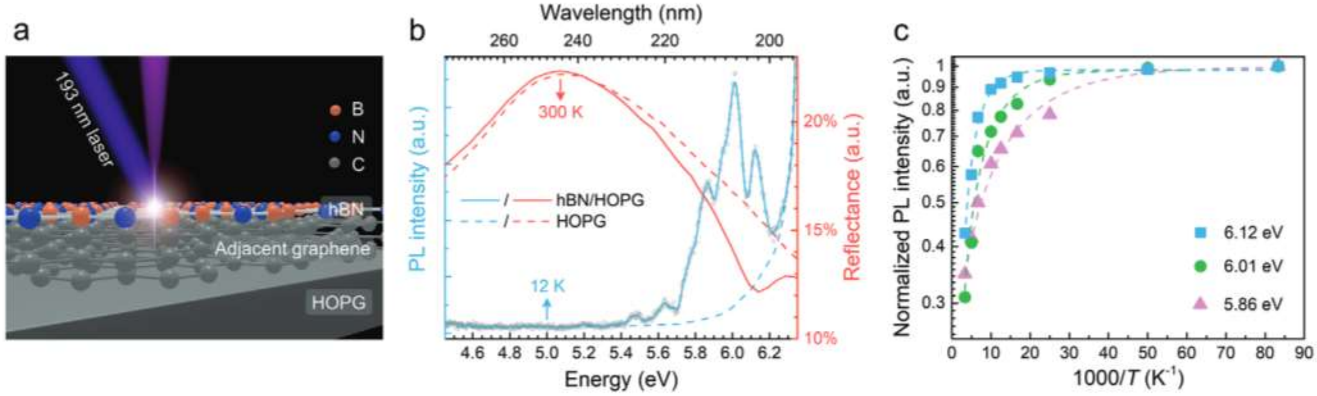

Figure 3. Evidence of deep-UV emission in epitaxial monolayer hBN. a) Schematic of the PL experiment performed on monolayer hBN/HOPG heterostructure of Figure 1g. b) Measured, time-integrated PL spectra (blue curves, 12 K) and reflectance spectra (red curves, 300 K) of monolayer hBN/HOPG heterostructure (solid curves) and HOPG substrate (dashed curves). The gray circles are the PL data for monolayer hBN/HOPG heterostructures, while the blue solid curve is the corresponding smoothed curve. c) Temperature dependence of PL-peak intensity normalized to its $T = 12$ K value for the hBN/HOPG heterostructure.

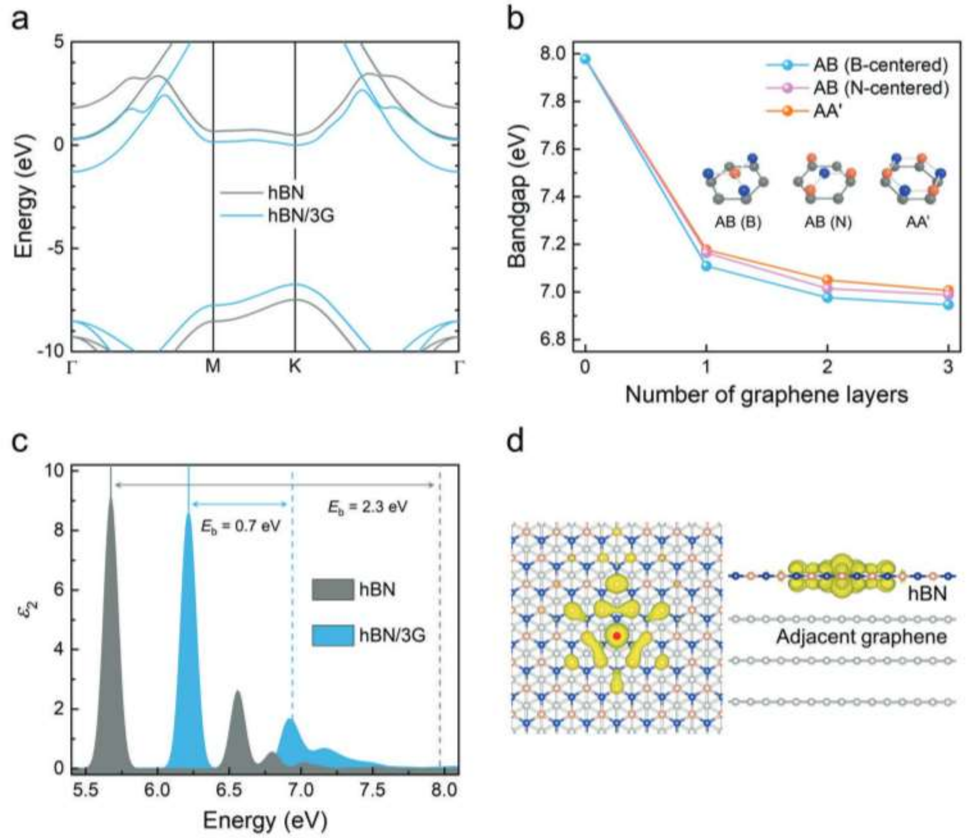

Figure 4. Giant bandgap renormalization of monolayer hBN on graphene. a) Quasiparticle band structure of freestanding monolayer hBN (gray curves) and monolayer hBN on three graphene layers (hBN/3G, blue curves). b) Calculated direct bandgap of monolayer hBN for a varying number of graphene layers. Insets: the three different stacking configurations used for the vertical hBN/G interface. c) Calculated absorption spectrum of a freestanding monolayer hBN (gray area) and monolayer hBN on three graphene layers (blue area). The vertical dashed lines indicate the quasiparticle bandgap, and the vertical solid lines show the 1s-exciton state position. d) Spatial map of the exciton wavefunction for the 1s-exciton state of monolayer hBN on three graphene layers: along the in-plane direction (left) and along the out-of-plane direction (right). The hole (red dot) is fixed slightly below a nitrogen atom. The isosurface is set to be [illegible]% of the maximum isovalue. The electron and hole distributions are well confined within the monolayer hBN region.

2.3. Theoretical Calculation and Analyses

In multilayer hBN with an indirect bandgap, all the previously reported emissions had peak energy lower than the indirect exciton (5.96 eV).[48–50] Recently, the emissions with higher peak energies (above 5.96 eV) were attributed to the carrier transition and recombination processes in monolayer hBN with a direct bandgap.[32,33,51] However, there is a large difference between the experimentally measured emission (6–6.15 eV)[32,33] and the theoretically predicted bandgap (8 eV) for a monolayer hBN.[34–36] To explain the 6.12 eV emission resonance from a monolayer hBN/HOPG heterostructure, we use first-principles calculations based on density functional theory (DFT) and many-body perturbation theory. We adopt the substrate-screening method to reflect the strong screening from the adjacent graphene layers underlying the monolayer hBN.[52–54] Details of the calculation method are included in Supporting Information (Figures S9–S12, Table S2, Supporting Information).

The computed band structure is presented in **Figure 4**a for a freestanding monolayer hBN (gray curves) versus monolayer hBN on three graphene layers (hBN/3G, blue curves). From this band structure, we construct the quasiparticle bandgap E_g of monolayer hBN on zero to three graphene layers, and present the result in Figure 4b. The zero graphene layer corresponds to the freestanding monolayer hBN, producing a direct $E_g = 7.98$ eV at $\mathbf{k} = \mathbf{K}$, in agreement with previous reports.[34–36] We find that adding graphene layers results in a giant bandgap renormalization of almost 1 eV for all simulated stacking configurations. Indeed, only two graphene layers are needed to converge the bandgap within 0.1 eV, which implies extreme screening of the Coulomb interaction by the underlying graphene layers. Thus, we attribute this giant bandgap renormalization to the metallic character of the graphene layers, also observed for other materials, such as MoS_2 and WSe_2.[45,55] This trend illustrates that the screening depends only on the adjacent graphene layers as previously reported for other vdW heterostructures.[56] Our predictions also agree well with the $E_g = 6.8 \pm 0.2$ eV recently measured with STM for monolayer hBN,[33] and the variation of the bandgap among different stacking configurations is small, less than 0.1 eV.

To explain the optical spectra and excitonic properties, we solve the Bethe–Salpeter equation including substrate-screening effects. Figure 4c shows the computed absorption spectrum for a monolayer hBN on three graphene layers (blue area) versus a freestanding monolayer hBN (gray area). The hBN/3G calculation produces a strong 1s-exciton resonance at 6.21 eV, close to the 6.12 eV peak of the measured PL spectrum (Figure 3b). We attribute the small difference (0.09 eV) between these energies to the zero-point energy renormalization, which is expected to be around 0.2 eV for bulk and freestanding monolayer hBN.[44,57] By comparing the exciton energy to the quasiparticle bandgap, we obtain a 0.7 eV exciton binding energy for hBN/3G, which is similar to the 0.7 eV binding energy of bulk hBN[43] and is much smaller than the 2.3 eV binding energy for freestanding monolayer hBN, reported also previously.[35] This huge reduction in binding energy also results from the metallic screening by the graphene layers.

We further study the 2D excitonic nature of the 6.21 eV-exciton resonance in Figure 4d by examining the exciton wavefunction. The 2D character of monolayer hBN is very clear because the wavefunction is strongly confined within the monolayer hBN. This result confirms the strong light-matter interactions associated with the measured 6.12 eV reflection and PL resonance (matching 6.21 eV of our computations) based on analysis in Figure 3. Thus, the measured reflection and emission peak at 6.12 eV indeed stems from the 1s-exciton state of monolayer hBN. This resonance is also distinguished clearly from the PL peaks of multilayer hBN, which are below 5.96 eV.[48–50] Furthermore, our calculated singlet–triplet splitting energy is 90 meV, similar to the value of bulk hBN[58] and also close to the splitting between the 6.12 and 6.01 eV peaks. This further supports that the PL signal at 6.01 eV is due to defect-induced triplet brightening.[32] Both the phonon replicas of monolayer hBN exciton and trion emissions and the phonon-assisted indirect exciton emissions of multilayer hBN[48–50] may contribute to the adjacent shoulders of the PL peak at 5.86 eV (Figure 3b), but not explored further in this work.

3. Conclusion

We have proposed and demonstrated an interface-mediated growth mechanism for the controlled epitaxy of monolayer hBN on graphene with superior structural, electrical, and optical properties. By implementing this approach, we have achieved a unidirectional, lateral epitaxy of monolayer hBN by controlling the energetically stable in-plane hBN/G interface formation. Moiré superlattice spanning the entire monolayer hBN with a single periodicity indicates a well lattice registry between hBN and underlying graphene without obvious rotation. Our experiment–theory comparison identifies that the deep-UV emission at 6.12 eV originates from the 1s-exciton state of monolayer hBN with a giant renormalized direct bandgap on graphene. This work provides a framework for the controllable epitaxy of monolayer hBN on graphene substrates and other 2D materials, offering a promising approach for the precise construction of both in-plane and out-of-plane monolayer heterointerfaces and heterostructures.

4. Experimental Section

Molecular Beam Epitaxy of hBN: hBN samples were grown using a Veeco GENxplor ultrahigh temperature MBE system equipped with a radio-frequency (RF) plasma-assisted nitrogen source and an integrated Telemark electron beam evaporator for boron (B). The growth conditions include B deposition rate of 0.01 Å s^{-1} and growth temperature in the range of 800–1600 °C. The growth temperatures mentioned in the context were the readings from the thermocouple of the substrate heater. Commercial 1 × 1 cm^2 HOPG from SPI Supplies with a mosaic spread of 0.8 ± 0.2° was used as substrate. A fresh surface was obtained by exfoliating the top surface of HOPG using adhesive tape. After exfoliation, the HOPG substrates were cleaned with acetone, methanol, and DI water. Before growth, the HOPG substrates were baked and degassed at 200 and 600 °C in the MBE load-lock chamber and preparation chamber for 2 h, respectively, to obtain a clean surface.

Morphological, Atomical, and Electrical Characterizations: The morphology of hBN was characterized using a Hitachi SU8000 SEM and a Bruker Dimension Icon AFM. The number of straight and jagged nanoribbons was counted under SEM across a 1000 µm × 25 µm area in five random regions of the 1 × 1 cm^2 hBN/HOPG samples. AFM measurements were carried out on the as-grown hBN/HOPG samples using TESPA-V2 cantilevers (from Bruker) in tapping-mode. STM experiments were performed at room-temperature under UHV conditions (2.0×10^{-10} Torr) with an RHK PanScan STM head with R9 control electronics. To desorb contamination from air exposure during storage, samples were exposed to 20 min of UV light in situ, which facilitated atomic-resolution imaging. STM images were acquired with an electrochemically etched PtIr tip with the STM feedback loop in constant current mode. Images were drift corrected using the Gywddion software package. cAFM measurements were performed on an NT-MDT Ntegra system using a conductive tip (Pt coated) HQ:NSC35/PT from Mikromasch with radius diameter being smaller than 30 nm. The height and current maps were recorded in contact mode with an applied tip bias of 0.01 V. Breakdown tests performed in the same system using a conductive tip with an extra layer of Pt (roughly 10 nm) were deposited using pulsed laser deposition to increase its conductivity and longevity.

Photoluminescence and Reflectance: The samples were mounted on the cold finger of a closed-cycle cryostat for temperature-dependent (12–300 K) measurements. A 193 nm pulsed excimer laser with a repetition rate of 100 Hz and a pulse energy of 0.2 mJ was used as excitation source. The emitted photons were spectrally resolved by a Horiba iHR550 spectrometer and detected through a Symphony II CCD detector. The reflectance was acquired using a Woollam M-2000 spectroscopic ellipsometer in the atmosphere and at room-temperature.

Theoretical Calculation: See details in the Supporting Information.

Supporting Information

Supporting Information is available from the Wiley Online Library or from the author.

Acknowledgements

P.W. and W.L. contributed equally to this work. This work was supported by the Army Research Office (ARO) (W911NF-17-1-0312), National Science Foundation (NSF) (DMR-1807984 and DMR-2118809), the Blue Sky Program in the College of Engineering at the University of Michigan, and the W. M. Keck Foundation. Computational resources were provided by the National Energy Research Scientific Computing (NERSC) Center, a U.S. Department of Energy (DOE) Office of Science User Facility supported under contract No. DE-AC02- 05CH11231. STM measurements were supported by funding from NSF QII-TAQS under award No. MPS-1936219. W.L. was partially supported by the Kwanjeong Educational Foundation Scholarship. D.Y.Q. was supported by the U.S. DOE Office of Science, Basic Energy Sciences, Materials Sciences, and Engineering Division under award No. DE-SC0021965. The authors are grateful to Prof. Jun Song and Yiqing Chen from McGill University for their discussions on growth dynamics.

Conflict of Interest

The authors declare no conflict of interest.

Data Availability Statement

The data that support the findings of this study are available from the corresponding author upon reasonable request.

Keywords

2D heterostructures, bandgap, graphene, moiré superlattices, monolayer hexagonal boron nitride

Received: February 11, 2022
Revised: March 20, 2022
Published online: April 21, 2022

[1] M. J. Allen, V. C. Tung, R. B. Kaner, *Chem. Rev.* **2010**, *110*, 132.
[2] K. Watanabe, T. Taniguchi, H. Kanda, *Nat. Mater.* **2004**, *3*, 404.
[3] A. K. Geim, I. V. Grigorieva, *Nature* **2013**, *499*, 419.
[4] X. Wang, F. Xia, *Nat. Mater.* **2015**, *14*, 264.
[5] M. Yankowitz, Q. Ma, P. Jarillo-Herrero, B. J. LeRoy, *Nat. Rev. Phys.* **2019**, *1*, 112.
[6] L. Britnell, R. V. Gorbachev, R. Jalil, B. D. Belle, F. Schedin, M. I. Katsnelson, L. Eaves, S. V. Morozov, A. S. Mayorov, N. M. Peres, *Nano Lett.* **2012**, *12*, 1707.
[7] A. H. Castro Neto, F. Guinea, N. M. R. Peres, K. S. Novoselov, A. K. Geim, *Rev. Mod. Phys.* **2009**, *81*, 109.
[8] A. F. Young, C. R. Dean, L. Wang, H. Ren, P. Cadden-Zimansky, K. Watanabe, T. Taniguchi, J. Hone, K. L. Shepard, P. Kim, *Nat. Phys.* **2012**, *8*, 550.
[9] L. Wang, Y. Gao, B. Wen, Z. Han, T. Taniguchi, K. Watanabe, M. Koshino, J. Hone, C. R. Dean, *Science* **2015**, *350*, 1231.
[10] A. Woessner, M. B. Lundeberg, Y. Gao, A. Principi, P. Alonso-González, M. Carrega, K. Watanabe, T. Taniguchi, G. Vignale, M. Polini, *Nat. Mater.* **2015**, *14*, 421.
[11] S. Bhowmick, A. K. Singh, B. I. Yakobson, *J. Phys. Chem. C* **2011**, *115*, 9889.
[12] J. Zhang, W. Xie, X. Xu, S. Zhang, J. Zhao, *Chem. Mater.* **2016**, *28*, 5022.
[13] D. Zhang, D.-B. Zhang, F. Yang, H.-Q. Lin, H. Xu, K. Chang, *2D Mater.* **2015**, *2*, 041001.
[14] C. Leon, M. Costa, L. Chico, A. Latgé, *Sci. Rep.* **2019**, *9*, 3508.
[15] S. Li, Z. Ren, J. Zheng, Y. Zhou, Y. Wan, L. Hao, *J. Appl. Phys.* **2013**, *113*, 033703.
[16] J. Mannhart, D. G. Schlom, *Science* **2010**, *327*, 1607.
[17] P. Yu, Y.-H. Chu, R. Ramesh, *Mater. Today* **2012**, *15*, 320.
[18] J. S. Lee, S. H. Choi, S. J. Yun, Y. I. Kim, S. Boandoh, J.-H. Park, B. G. Shin, H. Ko, S. H. Lee, Y.-M. Kim, *Science* **2018**, *362*, 817.
[19] L. Wang, X. Xu, L. Zhang, R. Qiao, M. Wu, Z. Wang, S. Zhang, J. Liang, Z. Zhang, Z. Zhang, *Nature* **2019**, *570*, 91.
[20] T.-A. Chen, C.-P. Chuu, C.-C. Tseng, C.-K. Wen, H.-S. P. Wong, S. Pan, R. Li, T.-A. Chao, W.-C. Chueh, Y. Zhang, *Nature* **2020**, *579*, 219.
[21] F. Liu, Y. Yu, Y. Zhang, X. Rong, T. Wang, X. Zheng, B. Sheng, L. Yang, J. Wei, X. Wang, X. Li, X. Yang, F. Xu, Z. Qin, Z. Zhang, B. Shen, X. Wang, *Adv. Sci.* **2020**, *7*, 2000917.
[22] Y.-J. Cho, A. Summerfield, A. Davies, T. S. Cheng, E. F. Smith, C. J. Mellor, A. N. Khlobystov, C. T. Foxon, L. Eaves, P. H. Beton, S. V. Novikov, *Sci. Rep.* **2016**, *6*, 34474.
[23] J. Meng, X. Zhang, Y. Wang, Z. Yin, H. Liu, J. Xia, H. Wang, J. You, P. Jin, D. Wang, *Small* **2017**, *13*, 1604179.
[24] G. Lu, T. Wu, P. Yang, Y. Yang, Z. Jin, W. Chen, S. Jia, H. Wang, G. Zhang, J. Sun, *Adv. Sci.* **2017**, *4*, 1700076.
[25] S. H. Lee, H. Jeong, O. F. N. Okello, S. Xiao, S. Moon, D. Y. Kim, G.-Y. Kim, J.-I. Lo, Y.-C. Peng, B.-M. Cheng, *Sci. Rep.* **2019**, *9*, 10590.
[26] D. A. Laleyan, K. Mengle, S. Zhao, Y. Wang, E. Kioupakis, Z. Mi, *Opt. Express* **2018**, *26*, 23031.
[27] X. Chen, H. Yang, B. Wu, L. Wang, Q. Fu, Y. Liu, *Adv. Mater.* **2019**, *31*, 1805582.
[28] J. Wrigley, J. Bradford, T. James, T. S. Cheng, J. Thomas, C. J. Mellor, A. N. Khlobystov, L. Eaves, C. T. Foxon, S. V. Novikov, *2D Mater.* **2021**, *8*, 034001.
[29] J. Gigliotti, X. Li, S. Sundaram, D. Deniz, V. Prudkovskiy, J.-P. Turmaud, Y. Hu, Y. Hu, F. Fossard, J.-S. Mérot, A. Loiseau, G. Patriarche, B. Yoon, U. Landman, A. Ougazzaden, C. Berger, W. A. d. Heer, *ACS Nano* **2020**, *14*, 12962.
[30] M. Yankowitz, J. Xue, D. Cormode, J. D. Sanchez-Yamagishi, K. Watanabe, T. Taniguchi, P. Jarillo-Herrero, P. Jacquod, B. J. LeRoy, *Nat. Phys.* **2012**, *8*, 382.
[31] G. Chen, A. L. Sharpe, P. Gallagher, I. T. Rosen, E. J. Fox, L. Jiang, B. Lyu, H. Li, K. Watanabe, T. Taniguchi, *Nature* **2019**, *572*, 215.
[32] C. Elias, P. Valvin, T. Pelini, A. Summerfield, C. Mellor, T. Cheng, L. Eaves, C. Foxon, P. Beton, S. Novikov, *Nat. Commun.* **2019**, *10*, 2639.
[33] R. J. P. Román, F. J. Costa, A. Zobelli, C. Elias, P. Valvin, G. Cassabois, B. Gil, A. Summerfield, T. S. Cheng, C. J. Mellor, *2D Mater.* **2021**, *8*, 044001.
[34] T. Galvani, F. Paleari, H. P. Miranda, A. Molina-Sánchez, L. Wirtz, S. Latil, H. Amara, F. Ducastelle, *Phys. Rev. B* **2016**, *94*, 125303.
[35] F. Ferreira, A. Chaves, N. Peres, R. Ribeiro, *J. Opt. Soc. Am. B* **2019**, *36*, 674.
[36] K. Mengle, E. Kioupakis, *APL Mater.* **2019**, *7*, 021106.
[37] P. Wang, A. Pandey, J. Gim, W. J. Shin, E. T. Reid, D. A. Laleyan, Y. Sun, D. Zhang, Z. Liu, Z. Zhong, R. Hovden, Z. Mi, *Appl. Phys. Lett.* **2020**, *116*, 171905.
[38] F. Liu, Z. Zhang, X. Rong, Y. Yu, T. Wang, B. Sheng, J. Wei, S. Zhou, X. Yang, F. Xu, Z. Qin, Y. Zhang, K. Liu, B. Shen, X. Wang, *Adv. Funct. Mater.* **2020**, *30*, 2001283.
[39] D. A. Laleyan, N. Fernández-Delgado, E. T. Reid, P. Wang, A. Pandey, G. A. Botton, Z. Mi, *Appl. Phys. Lett.* **2020**, *116*, 152102.
[40] F. Liu, X. Rong, Y. Yu, T. Wang, B. Sheng, J. Wei, S. Liu, J. Yang, F. Bertram, F. Xu, X. Yang, Z. Zhang, Z. Qin, Y. Zhang, B. Shen, X. Wang, *Appl. Phys. Lett.* **2020**, *116*, 142104.
[41] S. Liu, Y. Yuan, S. Sheng, T. Wang, J. Zhang, L. Huang, X. Zhang, J. Kang, W. Luo, Y. Li, H. Wang, W. Wang, C. Xiao, Y. Liu, Q. Wang, X. Wang, *J. Semicond.* **2021**, *42*, 122804.
[42] D. Wang, K. Uesugi, S. Xiao, K. Norimatsu, H. Miyake, *Appl. Phys. Express* **2020**, *13*, 095501.
[43] B. Arnaud, S. Lebègue, P. Rabiller, M. Alouani, *Phys. Rev. Lett.* **2006**, *96*, 026402.
[44] H. Mishra, S. Bhattacharya, *Phys. Rev. B* **2019**, *99*, 165201.
[45] F. Liu, M. E. Ziffer, K. R. Hansen, J. Wang, X. Zhu, *Phys. Rev. Lett.* **2019**, *122*, 246803.
[46] H. Yang, X. Wang, X. Li, *Phys. Rev. B* **2021**, *104*, 205307.
[47] G. Wang, A. Chernikov, M. M. Glazov, T. F. Heinz, X. Marie, T. Amand, B. Urbaszek, *Rev. Mod. Phys.* **2018**, *90*, 021001.
[48] G. Cassabois, P. Valvin, B. Gil, *Phys. Rev. B* **2016**, *93*, 035207.
[49] G. Cassabois, P. Valvin, B. Gil, *Nat. Photonics* **2016**, *10*, 262.
[50] E. Cannuccia, B. Monserrat, C. Attaccalite, *Phys. Rev. B* **2019**, *99*, 081109.
[51] A. Rousseau, L. Ren, A. Durand, P. Valvin, B. Gil, K. Watanabe, T. Taniguchi, B. Urbaszek, X. Marie, C. Robert, *Nano Lett.* **2021**, *21*, 10133.

[52] M. M. Ugeda, A. J. Bradley, S.-F. Shi, H. Felipe, Y. Zhang, D. Y. Qiu, W. Ruan, S.-K. Mo, Z. Hussain, Z.-X. Shen, *Nat. Mater.* **2014**, *13*, 1091.
[53] Z. -F. Liu, F. H. da Jornada, S. G. Louie, J. B. Neaton, *J. Chem. Theory Comput.* **2019**, *15*, 4218.
[54] D. Y. Qiu, F. H. da Jornada, S. G. Louie, *Nano Lett.* **2017**, *17*, 4706.
[55] S. Park, N. Mutz, T. Schultz, S. Blumstengel, A. Han, A. Aljarb, L.-J. Li, E. J. List-Kratochvil, P. Amsalem, N. Koch, *2D Mater.* **2018**, *5*, 025003.
[56] Y. Wang, S. Zhang, D. Huang, J. Cheng, Y. Li, S. Wu, *2D Mater.* **2016**, *4*, 015021.
[57] T. Vuong, S. Liu, A. Van der Lee, R. Cuscó, L. Artús, T. Michel, P. Valvin, J. Edgar, G. Cassabois, B. Gil, *Nat. Mater.* **2018**, *17*, 152.
[58] J. Koskelo, G. Fugallo, M. Hakala, M. Gatti, F. Sottile, P. Cudazzo, *Phys. Rev. B* **2017**, *95*, 035125.